Orientation dependence of high-order harmonic generation in graphene

Yuntian Zhang [1], Liang Li [1,*], Jiapeng Li,[1] Tengfei Huang,[1] Pengfei Lan,[1,†] and Peixiang Lu [1,2,3]

[1]*School of Physics and Wuhan National Laboratory for Optoelectronics,*
Huazhong University of Science and Technology, Wuhan 430074, China
[2]*Hubei Key Laboratory of Optical Information and Pattern Recognition, Wuhan Institute of Technology, Wuhan 430205, China*
[3]*CAS Center for Excellence in Ultra-intense Laser Science, Shanghai 201800, China*

We investigate the orientation dependence of high-order harmonic generation (HHG) in graphene by solving the semiconductor Bloch equations. The tight-binding approximation including up to the third-nearest-neighbor atoms is used to model the graphene. Our simulations show that the orientation dependence of HHG shows different patterns for different harmonics. With increasing the laser intensity, these patterns become similar except for a double-peak structure shown in lower-order harmonics. The double-peak structure appears at high laser intensity due to the contribution of the harmonic perpendicular to the laser polarization direction. The harmonic yield is decomposed as the contributions of the nearest-neighbor interaction, the second-nearest-neighbor interaction, and the third-nearest-neighbor interaction. Our results show that the harmonic yields are mainly contributed by the nearest-neighbor interaction, but the third-nearest-neighbor interaction also plays an important role and modifies the orientation dependence.

I. INTRODUCTION

Thanks to the advance of laser technology, the study of the interaction between strong laser fields and matter has attracted much attention. High-order harmonic generation (HHG) is one of the research hot spots. The study of HHG in atomic and molecular gases has resulted in great achievements and in the birth of attosecond science [1–5]. HHG in solids has been observed experimentally in the past few years [6–15]. There has been a growing interest in utilizing HHG in solids to probe the electronic band structures [11,16–20] and obtain coherent and bright attosecond pulses [11,21].

Recently, HHG in two-dimensional materials has become a new research frontier. Graphene is a representative two-dimensional material with great potential applications because of its unusual optical properties [22]. Several works have been done both theoretically [23–26] and experimentally [7,27–29]. Yoshikawa *et al.* reported that the HHG in graphene can be enhanced by elliptically polarized light [7]. Higuchi *et al.* demonstrated the manipulation of electrons in sub-optical-cycle timescales [27]. However, the model used to describe graphene in the previous works is the simplest tight-binding model that only considers the effect of the nearest-neighbor atoms [23–25,27]. When the intensity of the laser reaches the TW/cm^2 level, the effect of more distant neighbor atoms should be considered. The effect of the second-nearest-neighbor atoms and the third-nearest-neighbor atoms has not yet been discussed. In this work, we use the tight-binding model including up to third-nearest-neighbor

atoms to better describe graphene [30]. With this model, we can get more accurate energy bands and dipole transition moments analytically in the whole Brillouin zone.

The HHG efficiency is affected by the spatial structure of the crystal. This has the potential to probe the information of crystals. In recent years, the orientation dependence of HHG has been investigated in several crystals [10,31–41] like MgO [10,40,41] and ZnO [14,15,33,34,38]. The information contained in the orientation dependence is also helpful to understand the HHG process.

We numerically simulate the orientation dependence of HHG in graphene. The HHG process is decomposed as the contribution of the nearest-neighbor interaction, the second-nearest-neighbor interaction, and the third-nearest-neighbor interaction. Our results show that the third-nearest-neighbor interaction greatly affects the orientation dependence. Compared to previous works, our work provides a more complete perspective to understand the HHG process.

This paper is organized as follows. In Sec. II, we introduce the theoretical models we use in this work. The HHG process is numerically simulated. The results are shown in Sec. III. We decompose the harmonic in the directions parallel and perpendicular to the laser polarization directions. The two components are analyzed respectively. The summary and conclusions are given in Sec. IV.

II. THEORETICAL METHOD

A. The third-nearest-neighbor tight-binding model

Graphene is a two-dimensional material constituted of carbon atoms. As shown in Fig. 1(a), there are two different types of atoms in each primitive cell, labeled as

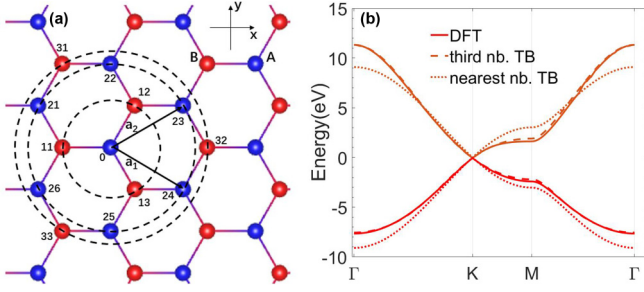*liangl@hust.edu.cn
†pengfeilan@hust.edu.cn

FIG. 1. (a) The structure of graphene. a_1 and a_2 denote the basis vectors of the primitive cell. The dashed cycles label the nearest-neighbor, the second-nearest-neighbor and the third-nearest-neighbor atoms, respectively. The numbers of atoms are labeled. (b) The band structure of graphene calculated by density functional theory (DFT), nearest-neighbor tight-binding approximation (nearest nb. TB), and third-nearest-neighbor tight-binding approximation (third nb. TB), respectively. K, M, and Γ points of the Brillouin zone are labeled.

A and B. Each atom has three nearest-neighbor atoms, six second-nearest-neighbor atoms, and three third-nearest-neighbor atoms [labeled by dashed cycles in Fig. 1(a)]. The distances between an atom and the nearest-, the second-nearest, and the third-nearest-neighbor atoms are 1.42, 2.46, and 2.84 Å, respectively. We consider the interaction with up to third-nearest-neighbor atoms in the tight-binding approximation. The p_z orbitals of the carbon atoms are considered.

In this third-nearest-neighbor tight-binding model, the basis vector $|\phi_{hk}\rangle$ is given by linear combinations of atomic orbital wave functions:

$$|\phi_{hk}\rangle = \sum_j e^{i\vec{k}\cdot\vec{R}_j}|\chi_{jh}\rangle, \qquad h = A, B \qquad (1)$$

$|\chi_{jh}\rangle$ is the atomic orbital wave function. A and B label the two types of atoms. j is the number of an atom, $j = 1l$ for the nearest-neighbor atoms, $j = 2l$ for the second-nearest-neighbor atoms, and $j = 3l$ for the third-nearest-neighbor atoms [as shown in Fig. 1(a)]. k is the crystal momentum. $\vec{R}_j$ is the position vector of an atom.

The overlap of atomic orbital wave functions is considered:

$$S_{AA} = \langle\phi_{Ak}|\phi_{Ak}\rangle = \langle\chi_{0A}|\chi_{0A}\rangle + \sum_{j=2l} e^{i\vec{k}\cdot\vec{R}_j}\langle\chi_{0A}|\chi_{jA}\rangle$$

$$= 1 + \sum_{j=2l} e^{i\vec{k}\cdot\vec{R}_j} s_1,$$

$$S_{AB} = \langle\phi_{Ak}|\phi_{Bk}\rangle = \sum_{j=1l} e^{i\vec{k}\cdot\vec{R}_j}\langle\chi_{0A}|\chi_{jB}\rangle$$

$$+ \sum_{j=3l} e^{i\vec{k}\cdot\vec{R}_j}\langle\chi_{0A}|\chi_{jB}\rangle$$

$$= \sum_{j=1l} e^{i\vec{k}\cdot\vec{R}_j} s_0 + \sum_{j=3l} e^{i\vec{k}\cdot\vec{R}_j} s_2. \qquad (2)$$

Here s_0, s_1, and s_2 are the parameters for the overlap between corresponding atomic orbital wave functions.

The interaction energies of the atoms are

$$H_{AA} = \langle\phi_{Ak}|\hat{H}|\phi_{Ak}\rangle$$

$$= \langle\chi_{0A}|\hat{H}|\chi_{0A}\rangle + \sum_{j=2l} e^{i\vec{k}\cdot\vec{R}_j}\langle\chi_{0A}|\hat{H}|\chi_{jA}\rangle$$

$$= \epsilon_{2p} + \sum_{j=2l} e^{i\vec{k}\cdot\vec{R}_j}\gamma_1,$$

$$H_{AB} = \langle\phi_{Ak}|\hat{H}|\phi_{Bk}\rangle$$

$$= \sum_{j=1l} e^{i\vec{k}\cdot\vec{R}_j}\langle\chi_{0A}|\hat{H}|\chi_{jB}\rangle$$

$$+ \sum_{j=3l} e^{i\vec{k}\cdot\vec{R}_j}\langle\chi_{0A}|\hat{H}|\chi_{jB}\rangle$$

$$= \sum_{j=1l} e^{i\vec{k}\cdot\vec{R}_j}\gamma_0 + \sum_{j=3l} e^{i\vec{k}\cdot\vec{R}_j}\gamma_2. \qquad (3)$$

Here γ_0, γ_1, and γ_2 are the parameters for the two-center hopping integrals between corresponding atoms. ϵ_{2p} is the energy of an atom itself.

To obtain the band structure of graphene, the time-independent Schrödinger equation is solved:

$$\hat{H}|\psi_{nk}\rangle = E_n|\psi_{nk}\rangle. \qquad (4)$$

The Bloch state $|\psi_{nk}\rangle$ can be expanded into

$$|\psi_{nk}\rangle = C_{nA}|\phi_{Ak}\rangle + C_{nB}|\phi_{Bk}\rangle. \qquad (5)$$

Using Eqs. (2), (3), (4), and (5), we can get

$$\begin{bmatrix} H_{AA} & H_{AB} \\ H_{AB}^* & H_{AA} \end{bmatrix}\begin{bmatrix} C_{nA} \\ C_{nB} \end{bmatrix} = E_n\begin{bmatrix} S_{AA} & S_{AB} \\ S_{AB}^* & S_{AA} \end{bmatrix}\begin{bmatrix} C_{nA} \\ C_{nB} \end{bmatrix}, \qquad (6)$$

where E_n is the energy of the system, $|\psi_n\rangle$ is the Bloch state, and $n = c$ and v means the conduction band and the valence band in this two-band model, respectively.

We can obtain the energy bands by solving the following equation:

$$\begin{vmatrix} H_{AA} - E_n S_{AA} & H_{AB} - E_n S_{AB} \\ H_{AB}^* - E_n S_{AB}^* & H_{AA} - E_n S_{AA} \end{vmatrix} = 0. \qquad (7)$$

The energy bands are

$$E_n(\vec{k}) = \frac{-(-2E_0 + E_1) \pm \sqrt{(-2E_0 + E_1)^2 - 4E_2 E_3}}{2E_3}. \qquad (8)$$

Several intermediate variables are defined as follows:

$$E_0 = H_{AA}S_{AA}, \qquad E_1 = S_{AB}H_{AB}^* + H_{AB}S_{AB}^*,$$

$$E_2 = H_{AA}^2 - H_{AB}H_{AB}^*, \qquad E_3 = S_{AA}^2 - S_{AB}S_{AB}^*, \qquad (9)$$

The expansion coefficient C_{nh} can be obtained as

$$C = \begin{bmatrix} C_{cA} & C_{vA} \\ C_{cB} & C_{vB} \end{bmatrix} = \begin{bmatrix} 1 & 1 \\ -\frac{H_{AA}-E_c S_{AA}}{H_{AB}-E_c S_{AB}} & -\frac{H_{AA}-E_v S_{AA}}{H_{AB}-E_v S_{AB}} \end{bmatrix}. \qquad (10)$$

To determine the seven unknown parameters in the model, we fit the energy bands calculated from density functional theory (DFT) [42]. The parameters are $\epsilon_{2p} = -0.28$ eV, $\gamma_0 = -2.97$ eV, $s_0 = 0.073$, $\gamma_1 = -0.073$ eV, $s_1 = 0.018$, $\gamma_2 = -0.33$ eV, and $s_2 = 0.026$. These parameters are the same as those in Ref. [30].

As shown in Fig. 1(b), the band structures of DFT and the nearest-neighbor tight-binding model agree well only in the area very close to the K point (Dirac point, zero band gaps) of the Brillouin zone. In the nearest-neighbor tight-binding

model, the valence band and the conduction band are completely symmetric, i.e., $E_c = -E_v$, but the band structure of DFT is not. The energy difference between the bands does not agree with that of DFT's [the dot-dashed line and the solid line in Fig. 1(b)]. For the third-nearest-neighbor tight-binding model, the band structure agrees well with the band structure of DFT in the whole Brillouin zone.

To numerically simulate the interaction between graphene and light, the dipole transition element $\vec{d}_{mn}(\vec{k})$ should be calculated:

$$d_{mn,\alpha}(\vec{k}) = i\langle u_{mk}|\partial_\alpha|u_{nk}\rangle, \qquad m, n = c, v. \tag{11}$$

Here $\alpha = x$ or y means the x or y component of the vector $\partial_\alpha = \frac{\partial}{\partial k_\alpha}$. $|u_{nk}\rangle$ is the periodical part of the Bloch state

$$\langle r|u_{nk}\rangle = e^{-i\vec{k}\cdot\vec{r}}\langle r|\psi_{nk}\rangle. \tag{12}$$

Because of the overlap of atomic orbital wave functions, the basis vectors in this tight-binding model are not orthogonal, i.e., $\langle\phi_{Ak}|\phi_{Ak}\rangle = S_{AA} \neq 0$ and $\langle\phi_{Ak}|\phi_{Bk}\rangle = S_{AB} \neq 0$. Substitute Eqs. (5) and (12) into Eq. (11) and we can get $\vec{d}_{mn}(\vec{k})$. The matrix composed of $\vec{d}_{mn}(\vec{k})$ is

$$D_\alpha = \begin{bmatrix} d_{cc,\alpha} & d_{cv,\alpha} \\ d_{vc,\alpha} & d_{vv,\alpha} \end{bmatrix}$$

$$= C^\dagger S(i\partial_\alpha N)N^{-1}C + (CN^{-1})^\dagger i\partial_\alpha(N^{-1}C). \tag{13}$$

Several intermediate variables are defined as follows:

$$S = \begin{bmatrix} S_{AA} & S_{AB} \\ S_{AB}^* & S_{AA} \end{bmatrix}, \tag{14}$$

$$N = \begin{bmatrix} S_{AA}^{-\frac{1}{2}} & -\frac{S_{AB}}{S_{AA}}S_1^{-\frac{1}{2}} \\ 0 & S_1^{-\frac{1}{2}} \end{bmatrix}, \tag{15}$$

$$S_1 = S_{AA} - \frac{S_{AB}S_{AB}^*}{S_{AA}}.$$

Because of the inversion symmetry of graphene, the Berry connection $\vec{d}_{cc}$ and $\vec{d}_{vv}$ can always become zero by choosing a proper gauge. In our numerical simulation $\vec{d}_{cc} = \vec{d}_{vv} = 0$. The dipole transition moment $\vec{d}_{cv} = \vec{d}_{vc}^*$.

B. Semiconductor Bloch equations

The semiconductor Bloch equations in the Bloch representation with the length gauge read as follows:

$$\frac{\partial\rho_{cv}(\vec{k}, t)}{\partial t} = \left[i(E_c - E_v) - \frac{1}{T_2}\right]\rho_{cv}(\vec{k}, t) + \vec{F}(t)\cdot\nabla_k\rho_{cv}(\vec{k}, t)$$
$$+ i\vec{F}(t)\cdot\vec{d}_{cv}[\rho_{vv}(\vec{k}, t) - \rho_{cc}(\vec{k}, t)], \tag{16}$$

$$\frac{\partial\rho_{vv}(\vec{k}, t)}{\partial t} = -\vec{F}(t)\cdot2\text{Im}[\vec{d}_{cv}\rho_{cv}(\vec{k}, t)] + \vec{F}(t)\cdot\nabla_k\rho_{vv}(\vec{k}, t). \tag{17}$$

Unless otherwise indicate, atomic units (a.u.) are used throughout: $e = \hbar = m_e = 1$, where e and m_e are the electron charge and mass, respectively. $\rho_{cc}(\vec{k})$ and $\rho_{vv}(\vec{k})$ are the populations in the conduction band and the valence band, respectively. $\rho_{cv}(\vec{k})$ is for the polarization between the two

bands. $\vec{F}(t)$ is the electric field of the laser pulse. The wavelength of the laser is 800 nm. The sine square envelope with 11 optical cycles (zero-to-zero) is used. In this work, the dephasing time $T_2 = 35$ fs for graphene [25].

In the numerical simulation, We sample the first Brillouin zone using a grid with 1501×1501 points along the directions of two basis vectors in the reciprocal space. We use the finite difference method to solve the time evolution process. The step size of the time-grid is 0.0303 a.u. (40 000 steps).

The current induced by the laser can be decomposed as the intraband current $\vec{J}_{\text{ra}}(t)$ and the interband current $\vec{J}_{\text{er}}(t)$:

$$\vec{J}_{\text{ra}}(t) = \sum_{n=c,v}\int_{BZ}\vec{v}_n\rho_{nn}(\vec{k}, t)dk_xdk_y, \tag{18}$$

$$\vec{J}_{\text{er}}(t) = -i\int_{BZ}[E_c(\vec{k}) - E_v(\vec{k})]\vec{d}_{cv}(k)\rho_{cv}(\vec{k}, t)d\vec{k} + \text{c.c.} \tag{19}$$

Here $\vec{v}_n(\vec{k}) = \nabla_k E_n(\vec{k})$ is the group velocity. The total current is

$$\vec{J}(t) = \vec{J}_{\text{ra}}(t) + \vec{J}_{\text{er}}(t). \tag{20}$$

The spectrum of harmonics can be obtained by calculating the absolute square of the Fourier-transformed total current:

$$I(\omega) \propto |\text{FT}[\vec{J}(t)]|^2. \tag{21}$$

III. RESULTS AND DISCUSSION

A. Orientation dependence of the harmonics

We calculate the orientation dependence of the HHG by scanning the polarization direction of the laser. The orientation dependencies of the third harmonic (H3), the fifth harmonic (H5), the seventh harmonic (H7), and the ninth harmonic(H9) are shown in Fig. 2. Because of the symmetry of the graphene only odd-order harmonics exist. The orientation dependence is sixfold symmetric, so we only need to discuss in one period from $60°$ to $120°$. For H3, the orientation dependence reaches its maximum at $90°$ when the laser intensities are 0.6 and 0.8 TW/cm^2. The double-peak structure appears when the laser intensity is 1.4 TW/cm^2. The peaks are at $75°$ and $105°$. For H5, the orientation dependence is nearly isotropic when the laser intensity is 0.6 TW/cm^2. There is a peak at $60°$ when the laser intensity is 0.8 TW/cm^2. A similar double-peak structure appears when the laser intensity is 1.4 TW/cm^2. The orientation dependence of H7 reaches its maximums at $60°$ or $90°$. The peak of the orientation dependence for H9 is at $60°$ for the three intensities. For different-order harmonics, when the laser intensity is 1.4 TW/cm^2, the peaks appear at $60°$ for all of these orientation dependencies except the double-peak structure.

To analyze the anisotropy of the harmonics, the contributions of the intraband current and the interband current are compared. Figure 3 shows the harmonic spectra when the laser polarization direction is at $60°$. Regardless of the change of laser intensities, the interband contribution is larger than the intraband contribution. The high-order harmonic spectra with other laser polarization directions show the same result. Therefore, the interband transition dominates the HHG process. From now on we only consider the interband current.
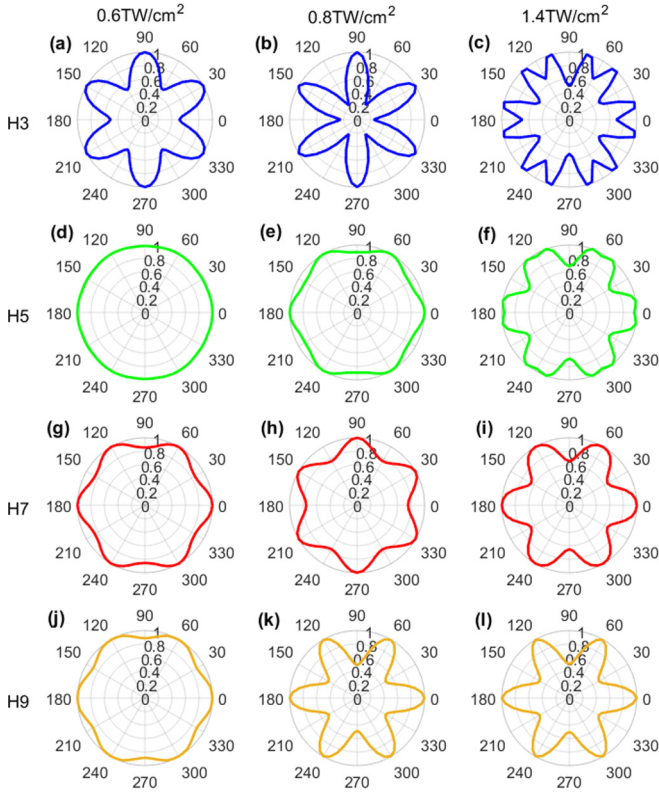
FIG. 2. The orientation dependence of the harmonics. The orientation angle is defined as the angle between the laser polarization direction and the x axis. The orientation dependencies of H3, H5, H7, and H9 are shown in different rows. Three laser intensities are used: 0.6, 0.8, and 1.4 TW/cm^2.

B. Contribution of the vertical current

We decompose the interband current in the directions parallel and perpendicular to the laser polarization directions:

$$\vec{J}_{\mathrm{er}}(t) = \vec{J}_{\mathrm{er}\parallel}(t) + \vec{J}_{\mathrm{er}\perp}(t). \quad (22)$$

First, we discuss the effect of the vertical current $\vec{J}_{\mathrm{er}\perp}(t)$. Figure 4 shows the orientation dependence corresponding to $\vec{J}_{\mathrm{er}\perp}(t)$. The peaks of the orientation dependence appear at 75° and 105°. For all the intensities, different-order harmonics show the same result.

As shown in Fig. 5, we compare the orientation dependence corresponding to the total current, the parallel current, and the vertical current for H3 and H5. The peak positions for the vertical current fit the double-peak structures. Only the peaks at 60° and 90° exist if we only consider the parallel component of the interband current. Therefore, the existence of the vertical current is responsible for the double-peak structure.

The vertical current at 75° and 105° can be explained by the structure of the dipole transition moment $\vec{d}_{cv}(\vec{k})$. The structure of $\vec{d}_{cv}(\vec{k})$ is shown in Fig. 6(a). As we can see, the large magnitudes of $\vec{d}_{cv}(\vec{k})$ appear around the K and the K' points (Dirac points), and the direction of $\vec{d}_{cv}(\vec{k})$ shows a circular vortex structure. Because the ionization rate is proportional to $\vec{F}(t) \cdot \vec{d}_{cv}(\vec{k})$, the transition between the energy bands mainly occurs in the areas perpendicular to the laser polarization di-
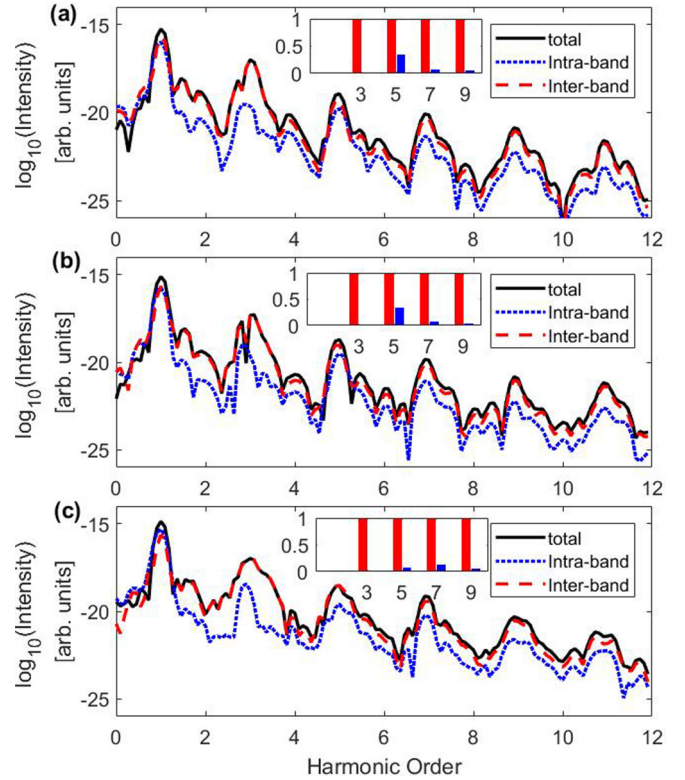

FIG. 3. High-order harmonic spectra with laser polarization direction at 60°: (a) at laser intensity 0.6 TW/cm^2, (b) at laser intensity 0.8 TW/cm^2, and (c) at laser intensity 1.4 TW/cm^2. The insets show the comparison of intraband and interband contributions. Regardless of the change of laser intensities, the interband contribution is larger than the intraband contribution.

rection near the K and K' points [gray area near the K point in Fig. 6(a)]. We only need to consider these areas. Moreover, the ionization rate dominates the change of the polarization between the bands, so $\rho_{cv}(\vec{k}, t) \propto \vec{F}(t) \cdot \vec{d}_{cv}(\vec{k})$. By substituting
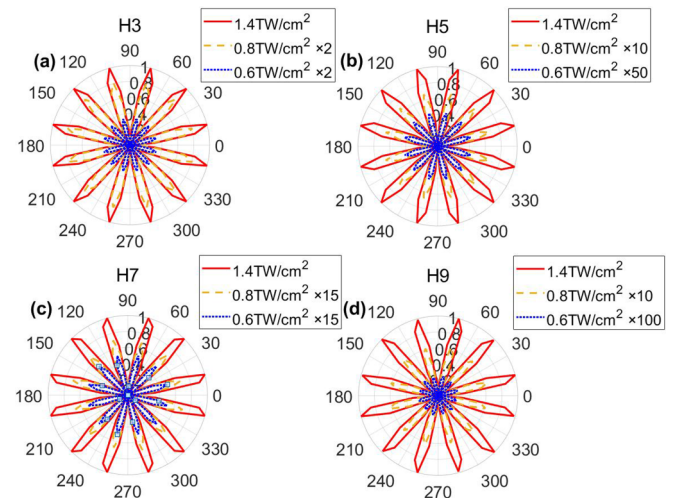

FIG. 4. Orientation dependence of the harmonics corresponding to the vertical interband current. The yields of the harmonics are scaled for a better look as shown in the legends.
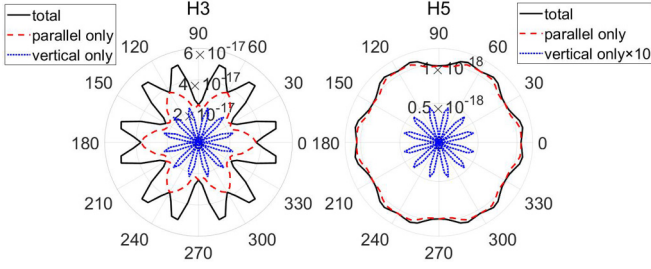
FIG. 5. Comparison of the orientation dependencies corresponding to the total current, the parallel current, and the vertical current for H3 and H5. The laser intensity is 1.4 TW/cm².

this relation into Eq. (19), the vertical interband current can be calculated. The maximums of the vertical interband currents $\vec{J}_{\mathrm{er}\perp}$ for different-order harmonics are shown in Fig. 6(b). Note that we consider all the areas where electrons can move in the first Brillouin zone. As shown in Fig. 6(b), the peaks of $\vec{J}_{\mathrm{er}\perp}$ for H3, H5, H7, and H9 all appear around 75° and 105°. These angles agree with the angles of the peaks in Fig. 4. Therefore, the structure of the dipole transition moment is responsible for the existence of the vertical interband current.

C. Effect of the neighbor atoms

Next, we consider the parallel component of the interband current. We can analyze the interaction of different kinds of neighbor atoms by decomposing the interband current:

$$\vec{J}_{\mathrm{er}\parallel}(t) = \vec{J}_{\mathrm{er}\parallel}^{1}(t) + \vec{J}_{\mathrm{er}\parallel}^{2}(t) + \vec{J}_{\mathrm{er}\parallel}^{3}(t), \qquad (23)$$

where $\vec{J}_{\mathrm{er}\parallel}^{1}(t)$, $\vec{J}_{\mathrm{er}\parallel}^{2}(t)$, and $\vec{J}_{\mathrm{er}\parallel}^{3}(t)$ are the parallel interband currents only contributed by the nearest-neighbor interaction, the second-nearest-neighbor interaction, and the third-nearest-neighbor interaction.

According to Eq. (19), the parallel component of the interband current $\vec{J}_{\mathrm{er}\parallel}(t)$ is affected by the dipole transition moment $\vec{d}_{cv}(\vec{k})$ and the energy band E_{n}. As is well known, the dipole transition moment $\vec{d}_{cv}(\vec{k})$ represent the ability of transition between the energy bands. In the third-nearest-neighbor
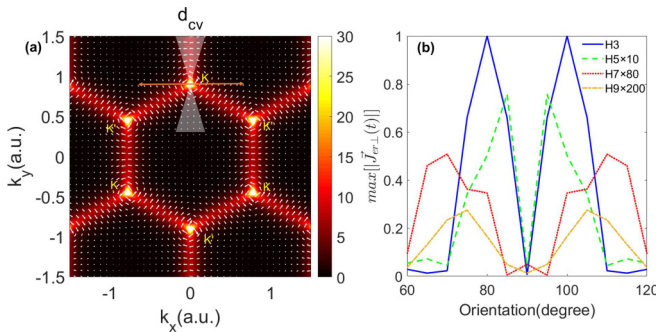

FIG. 6. (a) The dipole transition moment $\vec{d}_{cv}(\vec{k})$ of graphene. Color means the magnitude of $\vec{d}_{cv}(\vec{k})$ and arrows mean the direction of $\vec{d}_{cv}(\vec{k})$. The double-headed arrow means the laser polarization direction. The gray region is the main ionization area. (b) The maximum vertical interband current for each order harmonic as the function of the laser polarization direction when the laser intensity is 1.4 TW/cm².
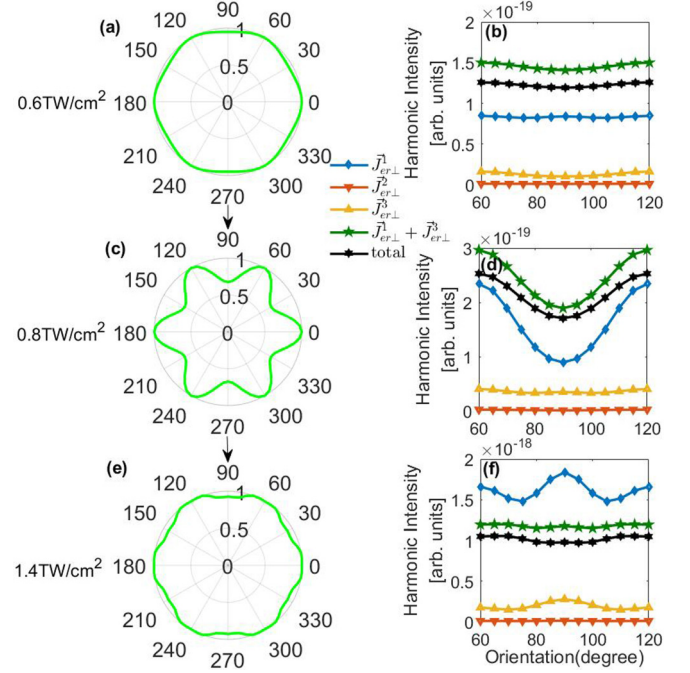

FIG. 7. Panels (a), (c), and (e) show the orientation dependence of H5 corresponding to the total current $\vec{J}_{\mathrm{er}\parallel}(t)$ at different laser intensities. Only the parallel component of the total interband current is considered. Panels (b), (d), and (f) show the orientation dependence corresponding to $\vec{J}_{\mathrm{er}\parallel}^{1}(t)$, $\vec{J}_{\mathrm{er}\parallel}^{2}(t)$, $\vec{J}_{\mathrm{er}\parallel}^{3}(t)$, $\vec{J}_{\mathrm{er}\parallel}^{1}(t) + \vec{J}_{\mathrm{er}\parallel}^{3}(t)$, and $\vec{J}_{\mathrm{er}\parallel}(t)$ at different laser intensities.

tight-binding model, $\vec{d}_{cv}(\vec{k})$ can be written as a function of the seven parameters, i.e., $\vec{d}_{cv}(\epsilon_{2p}, \gamma_{0}, s_{0}, \gamma_{1}, s_{1}, \gamma_{2}, s_{2})$. By setting part of the parameters to zeros, we can exclude the influence of the corresponding interaction. In detail, γ_{0} and s_{0} correspond to the nearest-neighbor interaction, γ_{1} and s_{1} correspond to the second-nearest-neighbor interaction, and γ_{2} and s_{2} correspond to the third-nearest-neighbor interaction. So $\vec{J}_{\mathrm{er}\parallel}^{1}(t)$, $\vec{J}_{\mathrm{er}\parallel}^{2}(t)$, and $\vec{J}_{\mathrm{er}\parallel}^{3}(t)$ can be defined as

$$\vec{J}_{\mathrm{er}\parallel}^{1}(t) = \vec{J}_{\mathrm{er}\parallel}[E_{c}, E_{v}, \vec{d}_{cv}(\epsilon_{2p}, \gamma_{0}, s_{0}, 0, 0, 0, 0)],$$

$$\begin{aligned} \vec{J}_{\mathrm{er}\parallel}^{2}(t) = &\vec{J}_{\mathrm{er}\parallel}[E_{c}, E_{v}, \vec{d}_{cv}(\epsilon_{2p}, \gamma_{0}, s_{0}, \gamma_{1}, s_{1}, 0, 0)] \\ &- \vec{J}_{\mathrm{er}\parallel}[E_{c}, E_{v}, \vec{d}_{cv}(\epsilon_{2p}, \gamma_{0}, s_{0}, 0, 0, 0, 0)], \quad (24) \end{aligned}$$

$$\begin{aligned} \vec{J}_{\mathrm{er}\parallel}^{3}(t) = &\vec{J}_{\mathrm{er}\parallel}[E_{c}, E_{v}, \vec{d}_{cv}(\epsilon_{2p}, \gamma_{0}, s_{0}, \gamma_{1}, s_{1}, \gamma_{2}, s_{2})] \\ &- \vec{J}_{\mathrm{er}\parallel}[E_{c}, E_{v}, \vec{d}_{cv}(\epsilon_{2p}, \gamma_{0}, s_{0}, \gamma_{1}, s_{1}, 0, 0)]. \end{aligned}$$

By calculating $\vec{J}_{\mathrm{er}\parallel}^{1}(t)$, $\vec{J}_{\mathrm{er}\parallel}^{2}(t)$, $\vec{J}_{\mathrm{er}\parallel}^{3}(t)$, and $\vec{J}_{\mathrm{er}\parallel}(t)$, the corresponding high-order harmonic spectrum and orientation dependence can be obtained. Figures 7(a), 7(c) and 7(e) show the orientation dependence of H5 corresponding to $\vec{J}_{\mathrm{er}\parallel}(t)$ at three laser intensities. The peaks of the orientation dependence are at 60°, but the peak-valley ratio is different. As shown in Figs. 7(b), 7(d) and 7(f), the biggest contribution comes from the nearest-neighbor interaction, i.e., $\vec{J}_{\mathrm{er}\parallel}^{1}(t)$. $\vec{J}_{\mathrm{er}\parallel}^{2}(t)$ contributes the least and is nearly isotropic, so it does
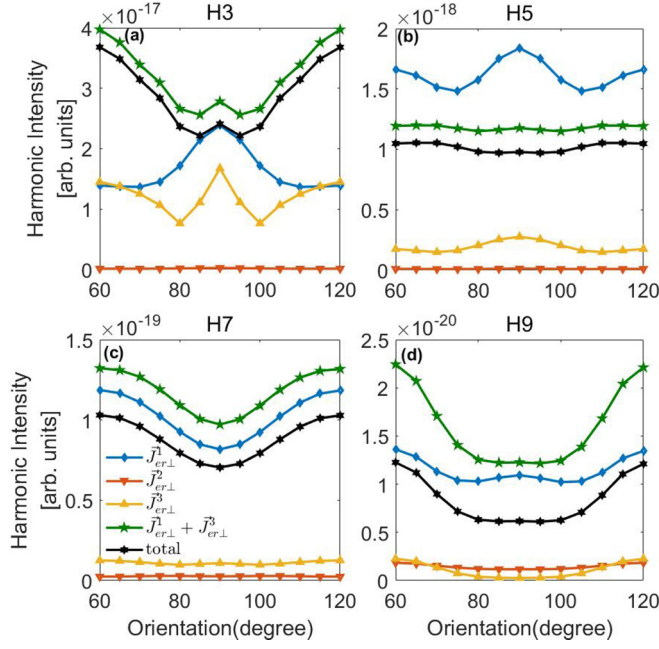
FIG. 8. The contribution of $\vec{J}_{\mathrm{er}\parallel}^1(t)$, $\vec{J}_{\mathrm{er}\parallel}^2(t)$, $\vec{J}_{\mathrm{er}\parallel}^3(t)$, $\vec{J}_{\mathrm{er}\parallel}^1(t) + \vec{J}_{\mathrm{er}\parallel}^3(t)$, and the total current $\vec{J}_{\mathrm{er}\parallel}(t)$ in the same intensity 1.4 TW/cm^2. Panels (a), (b), (c), and (d) show the results of different-order harmonics from H3 to H9, respectively. Only the parallel component of the total interband current is considered.

not change the orientation dependence. The minor contribution of $\vec{J}_{\mathrm{er}\parallel}^2(t)$ is because the overlaps between the atomic orbital wave functions s_1 and the two-center hopping integrals γ_1 are both small for the second-nearest-neighbor atoms. The contribution of the third-nearest-neighbor interaction, i.e., $\vec{J}_{\mathrm{er}\parallel}^3(t)$ is smaller than $\vec{J}_{\mathrm{er}\parallel}^1(t)$ but cannot be neglected. The orientation dependence could be modified by the interference between $\vec{J}_{\mathrm{er}\parallel}^1(t)$ and $\vec{J}_{\mathrm{er}\parallel}^3(t)$. We consider the result of 1.4 TW/cm^2 as an example. As we can see in Fig. 7(f), the peaks of the orientation dependence corresponding to $\vec{J}_{\mathrm{er}\parallel}^1(t)$ appear at both 60° and 90° (diamond blue line). Due to the interference between $\vec{J}_{\mathrm{er}\parallel}^1(t)$ and $\vec{J}_{\mathrm{er}\parallel}^3(t)$, the peak at 90° is suppressed. The orientation dependence corresponding to the total interband current $\vec{J}_{\mathrm{er}\parallel}(t)$ only shows the peaks at 60° (hexagonal black line), and the peak-valley ratio is smaller. To further verify this result, we calculate the sum of $\vec{J}_{\mathrm{er}\parallel}^1(t)$ and $\vec{J}_{\mathrm{er}\parallel}^3(t)$. If we consider the contribution of $\vec{J}_{\mathrm{er}\parallel}^1(t) + \vec{J}_{\mathrm{er}\parallel}^3(t)$ (pentagonal green line), the orientation dependence has the same structure as the total orientation dependence (hexagonal black line) except for the slightly different intensities. For

other laser intensities, as shown in Figs. 7(b) and 7(d), the orientation dependence corresponding to $\vec{J}_{\mathrm{er}\parallel}^1(t) + \vec{J}_{\mathrm{er}\parallel}^3(t)$ also has the same structure as the total orientation dependence.

Figure 8 shows the orientation dependence of H3, H5, H7, and H9 at 1.4 TW/cm^2. The biggest contribution still comes from $\vec{J}_{\mathrm{er}\parallel}^1(t)$. For different harmonic orders, the intensity ratios of $\vec{J}_{\mathrm{er}\parallel}^1(t)$, $\vec{J}_{\mathrm{er}\parallel}^2(t)$, and $\vec{J}_{\mathrm{er}\parallel}^3(t)$ are different. $\vec{J}_{\mathrm{er}\parallel}^2(t)$ is still isotropic and does not change the orientation dependence. The interference between $\vec{J}_{\mathrm{er}\parallel}^1(t)$ and $\vec{J}_{\mathrm{er}\parallel}^3(t)$ plays an important role in the orientation dependence. In Fig. 8(a), the orientation dependence corresponding to $\vec{J}_{\mathrm{er}\parallel}^1(t)$ only has a peak at 90°. The peaks appear at both 60° and 90° for the orientation dependence corresponding to $\vec{J}_{\mathrm{er}\parallel}^1(t) + \vec{J}_{\mathrm{er}\parallel}^3(t)$. This orientation dependence (pentagonal green line) also has the same structure as the total orientation dependence (hexagonal black line). The interference between $\vec{J}_{\mathrm{er}\parallel}^1(t)$ and $\vec{J}_{\mathrm{er}\parallel}^3(t)$ is important for H5, H7, and H9 as well.

IV. SUMMARY AND CONCLUSIONS

In summary, we investigate the orientation dependence of HHG in graphene. The tight-binding approximation considering the effect up to the third-nearest-neighbor atoms is used. Our results show that the effect of the second-nearest-neighbor atoms and the third-nearest-neighbor atoms cannot be neglected in order to obtain a more reliable band structure and dipole transition moment.

The HHG process is dominated by the interband current. To analyze our results, the interband current has been decomposed in the directions perpendicular and parallel to the laser polarization direction. The harmonics contributed by the perpendicular component of the interband current only appear around 75° and 105° regardless of the change of laser intensity. This result can be explained by the structure of the transition dipole moment. For the parallel component of the interband current, we decompose the interband current into the currents contributed by the nearest-neighbor interaction $\vec{J}_{\mathrm{er}\parallel}^1(t)$, the second-nearest-neighbor interaction $\vec{J}_{\mathrm{er}\parallel}^2(t)$, and the third-nearest-neighbor interaction $\vec{J}_{\mathrm{er}\parallel}^3(t)$. The contribution of $\vec{J}_{\mathrm{er}\parallel}^2(t)$ is small and nearly isotropic, so it does not change the relative harmonic intensity of different angles. The interference between $\vec{J}_{\mathrm{er}\parallel}^1(t)$ and $\vec{J}_{\mathrm{er}\parallel}^3(t)$ is the key to understanding the orientation dependence.

[1] F. Krausz and M. Ivanov, Rev. Mod. Phys. **81**, 163 (2009).

[2] F. Calegari, G. Sansone, S. Stagira, C. Vozzi, and M. Nisoli, J. Phys. B: At., Mol. Opt. Phys. **49**, 062001 (2016).

[3] P. Carpeggiani, M. Reduzzi, A. Comby, H. Ahmadi, S. Kühn, F. Calegari, M. Nisoli, F. Frassetto, L. Poletto, D. Hoff *et al.*, Nat. Photonics **11**, 383 (2017).

[4] D. Popmintchev, C. Hernández-García, F. Dollar, C. Mancuso, J. A. Pérez-Hernández, M.-C. Chen, A. Hankla, X. Gao, B. Shim, A. L. Gaeta *et al.*, Science **350**, 1225 (2015).

[5] P. M. Kraus, B. Mignolet, D. Baykusheva, A. Rupenyan, L. Horn, E. F. Penka, G. Grassi, O. I. Tolstikhin, J. Schneider, F. Jensen *et al.*, Science **350**, 790 (2015).

[6] S. Ghimire, A. D. DiChiara, E. Sistrunk, P. Agostini, L. F. DiMauro, and D. A. Reis, Nat. Phys. **7**, 138 (2011).

[7] N. Yoshikawa, T. Tamaya, and K. Tanaka, Science **356**, 736 (2017).

[8] O. Schubert, M. Hohenleutner, F. Langer, B. Urbanek, C. Lange, U. Huttner, D. Golde, T. Meier, M. Kira, S. W. Koch *et al.*, Nat. Photonics **8**, 119 (2014).

[9] F. Langer, M. Hohenleutner, U. Huttner, S. W. Koch, M. Kira, and R. Huber, Nat. Photonics **11**, 227 (2017).

[10] Y. S. You, D. A. Reis, and S. Ghimire, Nat. Phys. **13**, 345 (2017).

[11] T. T. Luu, M. Garg, S. Y. Kruchinin, A. Moulet, M. T. Hassan, and E. Goulielmakis, Nature (London) **521**, 498 (2015).

[12] G. Ndabashimiye, S. Ghimire, M. Wu, D. A. Browne, K. J. Schafer, M. B. Gaarde, and D. A. Reis, Nature (London) **534**, 520 (2016).

[13] H. Liu, Y. Li, Y. S. You, S. Ghimire, T. F. Heinz, and D. A. Reis, Nat. Phys. **13**, 262 (2017).

[14] Y.-F. Zhang, T.-F. Huang, J.-P. Li, K. Yang, L. Li, X.-S. Zhu, P.-F. Lan, and P.-X. Lu, Chinese Phys. B **30**, 074204 (2021).

[15] L. Li, T. Huang, P. Lan, Y. Zhang, J. Li, X. Zhu, L. He, W. Cao, and P. Lu, arXiv:2010.13298.

[16] G. Vampa, T. J. Hammond, N. Thiré, B. E. Schmidt, F. Légaré, C. R. McDonald, T. Brabec, D. D. Klug, and P. B. Corkum, Phys. Rev. Lett. **115**, 193603 (2015).

[17] A. Lanin, E. Stepanov, A. Fedotov, and A. Zheltikov, Optica **4**, 516 (2017).

[18] N. Tancogne-Dejean, O. D. Mücke, F. X. Kärtner, and A. Rubio, Phys. Rev. Lett. **118**, 087403 (2017).

[19] M. Hohenleutner, F. Langer, O. Schubert, M. Knorr, U. Huttner, S. W. Koch, M. Kira, and R. Huber, Nature (London) **523**, 572 (2015).

[20] L. Li, P. Lan, L. He, W. Cao, Q. Zhang, and P. Lu, Phys. Rev. Lett. **124**, 157403 (2020).

[21] M. Garg, M. Zhan, T. T. Luu, H. Lakhotia, T. Klostermann, A. Guggenmos, and E. Goulielmakis, Nature (London) **538**, 359 (2016).

[22] A. H. Castro Neto, F. Guinea, N. M. R. Peres, K. S. Novoselov, and A. K. Geim, Rev. Mod. Phys. **81**, 109 (2009).

[23] S. Jiang, H. Wei, J. Chen, C. Yu, R. Lu, and C. D. Lin, Phys. Rev. A **96**, 053850 (2017).

[24] M. S. Mrudul and G. Dixit, Phys. Rev. B **103**, 094308 (2021).

[25] C. Liu, Y. Zheng, Z. Zeng, and R. Li, Phys. Rev. A **97**, 063412 (2018).

[26] S. A. Sato, H. Hirori, Y. Sanari, Y. Kanemitsu, and A. Rubio, Phys. Rev. B **103**, L041408 (2021).

[27] T. Higuchi, C. Heide, K. Ullmann, H. B. Weber, and P. Hommelhoff, Nature (London) **550**, 224 (2017).

[28] C. Heide, T. Higuchi, H. B. Weber, and P. Hommelhoff, Phys. Rev. Lett. **121**, 207401 (2018).

[29] Y. Cheng, H. Hong, H. Zhao, C. Wu, Y. Pan, C. Liu, Y. Zuo, Z. Zhang, J. Xie, J. Wang *et al.*, Nano Lett. **20**, 8053 (2020).

[30] S. Reich, J. Maultzsch, C. Thomsen, and P. Ordejon, Phys. Rev. B **66**, 035412 (2002).

[31] J. Li, Q. Zhang, L. Li, X. Zhu, T. Huang, P. Lan, and P. Lu, Phys. Rev. A **99**, 033421 (2019).

[32] Y. Sanari, H. Hirori, T. Aharen, H. Tahara, Y. Shinohara, K. L. Ishikawa, T. Otobe, P. Xia, N. Ishii, J. Itatani, S. A. Sato, and Y. Kanemitsu, Phys. Rev. B **102**, 041125(R) (2020).

[33] S. Jiang, J. Chen, H. Wei, C. Yu, R. Lu, and C. D. Lin, Phys. Rev. Lett. **120**, 253201 (2018).

[34] S. Gholam-Mirzaei, J. Beetar, and M. Chini, Appl. Phys. Lett. **110**, 061101 (2017).

[35] J.-Z. Jin, X.-R. Xiao, H. Liang, M.-X. Wang, S.-G. Chen, Q. Gong, and L.-Y. Peng, Phys. Rev. A **97**, 043420 (2018).

[36] S. Jiang, S. Gholam-Mirzaei, E. Crites, J. E. Beetar, M. Singh, R. Lu, M. Chini, and C. Lin, J. Phys. B: At., Mol. Opt. Phys. **52**, 225601 (2019).

[37] K. Kaneshima, Y. Shinohara, K. Takeuchi, N. Ishii, K. Imasaka, T. Kaji, S. Ashihara, K. L. Ishikawa, and J. Itatani, Phys. Rev. Lett. **120**, 243903 (2018).

[38] T.-Y. Du, Opt. Lett. **46**, 2007 (2021).

[39] Y. Bai, F. Fei, S. Wang, N. Li, X. Li, F. Song, R. Li, Z. Xu, and P. Liu, Nat. Phys. **17**, 311 (2021).

[40] M. Wu, Y. You, S. Ghimire, D. A. Reis, D. A. Browne, K. J. Schafer, and M. B. Gaarde, Phys. Rev. A **96**, 063412 (2017).

[41] L. Li, Y. Zhang, P. Lan, T. Huang, X. Zhu, C. Zhai, K. Yang, L. He, Q. Zhang, W. Cao *et al.*, Phys. Rev. Lett. **126**, 187401 (2021).

[42] Y. Tan, M. Povolotskyi, T. Kubis, Y. He, Z. Jiang, G. Klimeck, and T. B. Boykin, J. Comput. Electron. **12**, 56 (2013).